Giant Magnetoresistive Biosensor Array for Detecting Magnetorelaxation

Xiahan Zhou, *Student Member, IEEE*, Chih-Cheng Huang, and Drew A. Hall, *Member, IEEE*

***Abstract*—In this paper, a time-domain magnetorelaxometry biosensing scheme is presented using giant magnetoresistive (GMR) sensors to measure the fast relaxation response of superparamagnetic magnetic nanoparticles (MNPs) in a pulsed magnetic field. The system consists of an 8 × 10 GMR sensor array, a Helmholtz coil, an electromagnet driver, and an integrator-based analog front-end needed to capture the fast relaxation dynamics of MNPs. A custom designed electromagnet driver and Helmholtz coil improve the switch-off speed to >5 Oe/μs, limiting the dead zone time to <10 μs, and thus enables the system to monitor fast relaxation processes of 30 nm MNPs. A magnetic correlated double sampling technique is proposed to reduce sensor-to-sensor variation by 99.98% while also reducing temperature drift, circuit offset, and nonlinearity below the noise level. An optimum integration time is calculated and experimentally verified to maximize the SNR. Experiments with dried MNPs have shown successful relaxation detection, and immunoassay experiments have demonstrated their binding kinetics.**

***Index Terms*—Electromagnet driver, magnetorelaxometry biosensing, magnetic correlated double sampling, magnetic nanoparticles, magnetoresistive sensors.**

I. Introduction

RECENTLY, magnetic sensors that have been traditionally utilized in industrial applications are being used more and more in medical applications, such as point-of-care (POC) *in-vitro* diagnostics [1]–[15]. In magnetic biosensing, biomarkers (e.g., proteins, nucleic acids, cells, etc.) are tagged with magnetic nanoparticles (MNPs) and detected by magnetic sensors to diagnose and track the progression of diseases [4]–[15]. Fig. 1(a) shows one such example where a magnetic immunoassay is utilized for protein detection. The biomarker of interest is selectively captured by an antibody immobilized on the surface of the sensor and subsequently bound to a detection antibody conjugated with a MNP. By quantifying the number of MNPs tethered to the magnetic sensor, one can infer the concentration of biomarkers present in the sample.

Several types of magnetic sensors have been successfully used to detect magnetically labelled biomarkers. Nuclear magnetic resonance (NMR) sensors [3], [4] measure the bulk spin-spin relaxation time (T_2) of water molecules to indirectly detect magnetic clusters. Hall-effect sensors [9] measure the Hall voltage arising from bound magnetic beads. MNPs have also been shown to induce frequency shifts in LC resonators [10]. Among the many magnetic sensors available, giant magnetoresistive (GMR) devices standout for this application due to their high transduction efficiency, particularly at low magnetic fields [16], [17]. Traditionally, the MNPs tethered to the sensor surface have been detected by the local perturbation in the magnetic field [18]–[21]. While very sensitive, this technique requires high magnetic field uniformity, complex modulation schemes to deal with the low signal to baseline ratio, and long measurement time needed to reduce the noise.

Here, we propose an alternative temporal detection scheme, magnetorelaxometry (MRX), using a pulsed magnetic field, as shown in Fig. 1. Without an applied magnetic field, the magnetic moments of the superparamagnetic MNPs are randomly distributed resulting in zero net magnetic field. In Phase I, an external magnetic field H_A is applied, magnetizing and aligning the MNPs with the applied field. The underlying GMR sensor detects both the external field and the stray field from the MNPs, as denoted by the change in resistance. In Phase II, H_A is quickly removed resulting in Néel and/or Brownian relaxation

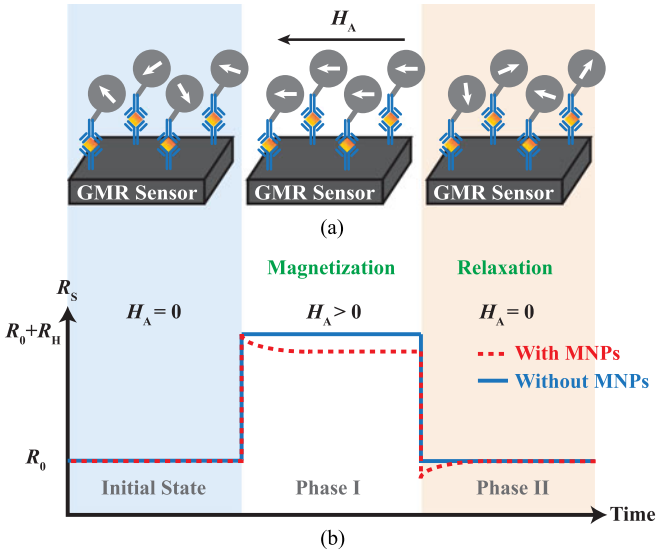

Fig. 1. Magnetorelaxometry biosensing concept. (a) A sandwich complex of antibody, antigen, antibody, and MNP bound on the sensor surface. (b) GMR sensor response due to a pulsed magnetic field.

Manuscript received August 30, 2016; revised December 26, 2016; accepted February 9, 2017. Date of publication June 2, 2017; date of current version July 26, 2017. This work was supported in part by the National Science Foundation under Grant ECCS-1454608 and in part by Qualcomm. This paper was recommended by Associate Editor M. Zaghloul.

The authors are with the Department of Electrical and Computer Engineering, University of California, San Diego, CA 92093 USA (e-mail: xiz250@ucsd.edu; chh033@eng.ucsd.edu; drewhall@ucsd.edu).

Color versions of one or more of the figures in this paper are available online at http://ieeexplore.ieee.org.

Digital Object Identifier 10.1109/TBCAS.2017.2682080

1932-4545 © 2017 IEEE. Personal use is permitted, but republication/redistribution requires IEEE permission.
See http://www.ieee.org/publications_standards/publications/rights/index.html for more information.

of the MNPs. For Brownian relaxation, the magnetization vectors undergo rigid rotation of the whole particle due to Brownian motion [22]. However, the MNPs here are tethered to the surface and thus have limited movement [23]. Instead, the MNPs must undergo Néel relaxation, where internal domain movement results in gradual randomization of the moment [24]. Note that the GMR sensor also exhibits Néel relaxation, but is orders of magnitude faster than the MNPs, allowing one to use the relaxation signature to detect the number of tethered MNPs. Compared with traditional magnetometry, which measures the absolute sensor resistance difference during Phase I, MRX shifts the burden from accuracy in amplitude to accuracy in time, relaxing the requirement on external field uniformity. Furthermore, since the relaxation of the MNPs is usually fast (nanosecond to millisecond time scale), MRX has both a shorter measurement time and the flexibility to tradeoff sensitivity with measurement time by adjusting the number of averaging cycles. Lastly, MRX is capable of distinguishing different types of MNPs on multi-labelled biomarkers due to their different relaxation times.

The MNP magnetization as a function of time can be written as follows [25]:

$$M_{\mathrm{N}}(\mathrm{t}) = C \cdot \ln\left(1 + \frac{t_{\mathrm{C}}}{t}\right) \tag{1}$$

where t is the time after switching off the applied field, t_{C} is the characteristic time that depends on the magnetization time and the field strength, and C is a scaling factor that depends on the surface coverage, magnetic viscosity, and initial magnetization.

This relaxation phenomenon can be measured either in the frequency- or time-domain. Frequency-domain MRX measures the complex magnetic susceptibility as function of frequency in an alternating magnetic field [26], whereas time-domain MRX directly measures the relaxation signal in response to a pulsed magnetic field [27], [28]. One of the significant challenges in time-domain relaxation is the need to collapse the applied magnetic field faster than the relaxation of the MNPs, which can be in the nanosecond to millisecond range depending on the size and material composition of the MNPs [29]–[31].

In this paper, a time-domain integrator-based MRX biosensing system is proposed. A magnetic correlated double sampling (MCDS) technique is applied to eliminate sensor-to-sensor variation, temperature drift, circuit offset, and non-linearity. We also designed an ultrafast electromagnet driver, which uses a large negative voltage to discharge the electromagnet and improve the switch-off speed to >5 Oe/μs.

The rest of this paper is organized as follows: Section II describes the proposed circuit architecture, Section III provides implementation details, and Section IV discusses testing methods and measurement results. Lastly, conclusions are drawn in Section V.

II. System Architecture and Circuit Design

A. System Architecture

A block diagram of the proposed MRX detector is shown in Fig. 2. A PC provides a user-defined magnetization time and magnetic field amplitude to the PC-FPGA interface. The

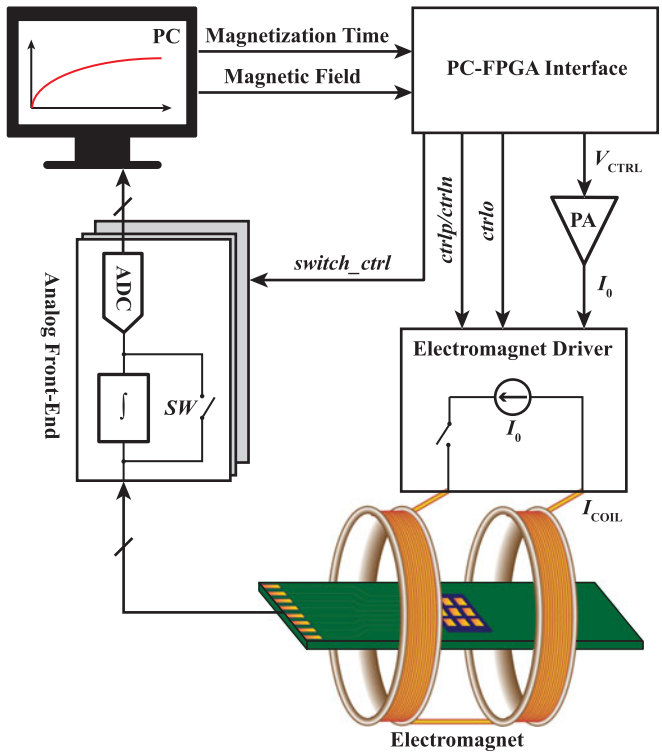

Fig. 2. Block diagram of the proposed relaxation detection system.

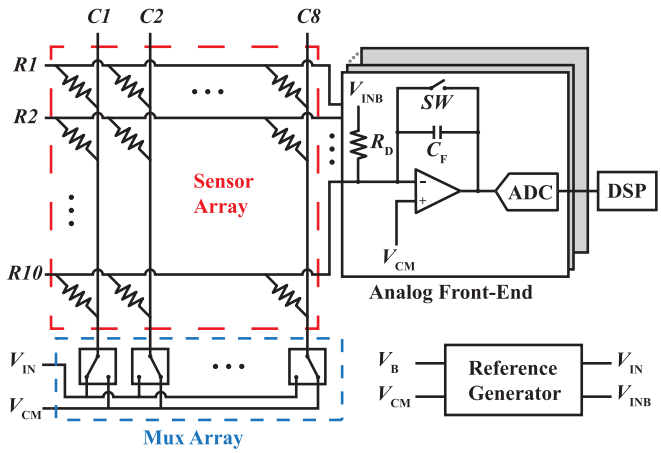

Fig. 3. Sensor array and readout architecture.

FPGA controls the timing of the electromagnet and readout circuitry. The power amplifier (PA) provides a DC current I_0 to the electromagnet driver that delivers a pulsed current I_{COIL} to the Helmholtz coil, generating a pulsed magnetic field for the sensor chip located in the center. The analog front-end (AFE) captures the resulting sensor response and transfers the data to the PC for post-processing.

The architecture of the AFE is illustrated in Fig. 3. The 8 × 10 GMR sensor array is arranged in a matrix with shared columns and rows. All the columns are connected to a column switching matrix that connects one column to V_{IN} and all others to a common-mode voltage, V_{CM}. Each of the rows is connected to a

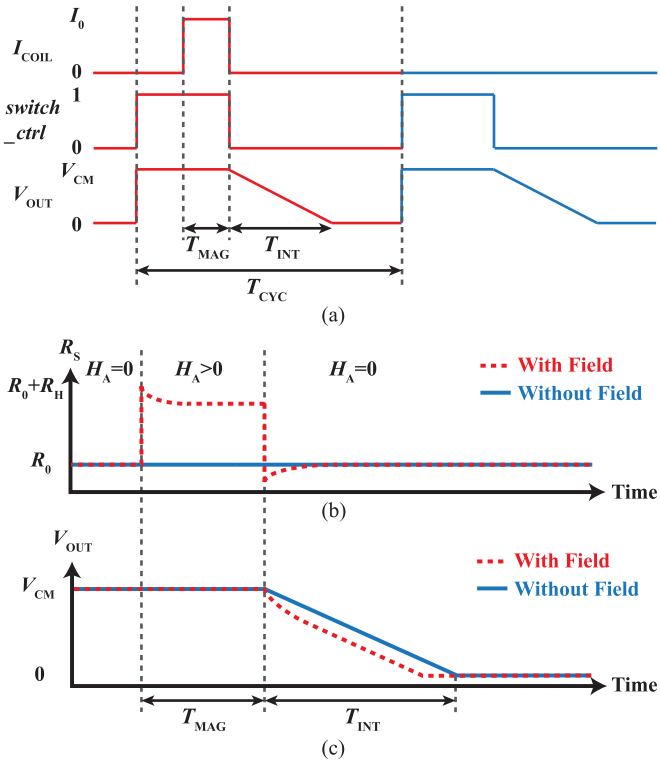

Fig. 4. (a) Timing diagram of coil current, integrator switch control, and integrator output voltage. (b) Sensor response and (c) corresponding integrator output using the MCDS scheme with and without a field applied.

readout circuit consisting of a switched integrator, an antialiasing filter, and an analog to digital converter (ADC). The reference generator produces voltages $V_{\rm IN}$ and $V_{\rm INB}$ as $V_{\rm CM}+V_{\rm B}$ and $V_{\rm CM}-V_{\rm B}$, which are used in the switched integrators as will be discussed later.

B. Magnetic Correlated Double Sampling

Detecting the minute relaxation signal in the presence of a large background signal is challenging. Traditional techniques, such as a Wheatstone bridge [17]–[19], require matched reference sensors to reject the background signal as common-mode. However, this approach is very sensitive to sensor-to-sensor variation and temperature drift, both of which are challenging to control for GMR sensors [32]. Moreover, circuit imperfections, such as amplifier offset and non-linearity, can further limit the sensitivity of the whole system. To extract the relaxation signal from these error sources, a MCDS technique is applied, as shown in Fig. 4. The magnetic field is initially off and the integrator reset switch *SW* is closed. Then, the magnetic field is turned on for a duration of $T_{\rm MAG}$, while *SW* remains closed (leaving the op-amp in unity gain configuration), therefore $V_{\rm OUT}=V_{\rm CM}$. Next, the magnetic field is turned off and the reset switch is opened simultaneously, resulting in $V_{\rm OUT}$ decaying. The integration time $T_{\rm INT}$ is determined by the sensor resistance R_0 and thus can be different due to sensor-to-sensor variation. This process is repeated in the subsequent cycle, except that the magnetic field remains off. Thus, the first cycle has the magnetic relaxation signal whereas the second does not.

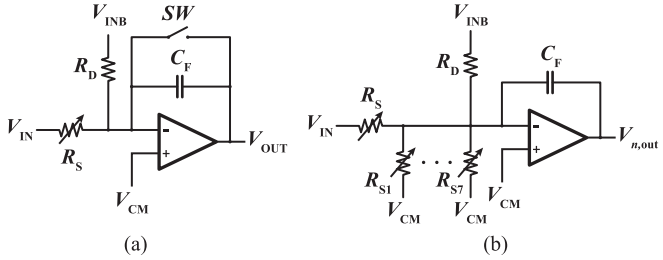

Fig. 5. (a) Switched integrator schematic and (b) equivalent schematic for noise analysis.

The sensor response and $V_{\rm OUT}$ in both cycles are shown in Fig. 4(b) and (c), respectively. When the magnetic field is turned off, the sensor resistance returns to the nominal resistance R_0 due to the relaxation of the MNPs. Therefore, instead of linear decay of $V_{\rm OUT}$ in the case without the field, $V_{\rm OUT}$ is distorted at the beginning of integration and returns to linear decay when the relaxation of the MNPs is completed. By subtracting $V_{\rm OUT}$ with and without the field, the integrated relaxation signal can be extracted.

This technique removes the sensor-to-sensor variation since each sensor is compared to itself instead of a reference sensor. While temperature may cause sensor resistance drift over time, the change is very slow compared to the period of cycle $T_{\rm CYC}$. Therefore, MCDS is able to reduce the effect of temperature drift dramatically without the need for other temperature compensation techniques [32]. By selecting $T_{\rm CYC}$ as a multiple of the power line frequency, the 60 Hz interference in the two adjacent cycles will be in phase and thus rejected as well. This technique is also effective at eliminating errors such as the circuit offset and non-linearity since these errors are consistent in every cycle.

C. Switched Integrator

In prior work, time-domain relaxation measurement techniques used amplifiers to detect the relaxation signal with Hall effect sensors [27], [28]. However, since the relaxation signal is largest at the time when the external field is turned off and gradually decreases with time, traditional amplifier-based relaxometry requires a high sampling-rate ADC to capture the dynamics. Since a high-resolution ADC is often needed to reduce the quantization error, integrators are applied to relax the bandwidth requirement of the ADC by integrating the relaxation signal with time, thus the integrated signal increases with time. The switched integrator circuit is shown in Fig. 5(a). It consists of an op-amp with capacitive feedback, a reset switch, and a current cancellation resistor at the input. Since GMR sensors typically have magnetoresistance ratios between 6–25% [17], there will be a substantial portion of the current flowing into the integrator that does not respond to the magnetic field and would limit the dynamic range. To remedy this issue, we have added a cancellation network that consists of resistor $R_{\rm D}$ that bleeds off part of the baseline current allowing us to use a smaller feedback capacitor $C_{\rm F}$ for the same integration time $T_{\rm INT}$. $R_{\rm D}$

is selected ∼10% lower than the nominal sensor resistance R_0 to account for process variation, and $V_{\rm IN} = V_{\rm CM} + V_{\rm B}$ and $V_{\rm INB} = V_{\rm CM} - V_{\rm B}$ where $V_{\rm CM}$ is a fixed common-mode voltage and $V_{\rm B}$ is an adjustable bias voltage. Consequently, in the integration phase, the output voltage $V_{\rm OUT}$ can be written as follows:

$$V_{OUT} = V_{\rm CM} - \frac{1}{C_{\rm F}} \int \frac{V_B}{R_0 + \Delta R\,(t)} - \frac{V_B}{R_D} dt \qquad (2)$$

where t is the time, and $\Delta R(t)$ represents the sensor response due to the MNP relaxation.

The relaxation signal after MCDS, $\Delta V_{\rm OUT}$, can be derived as follows based on the assumption that $R_0 \gg \Delta R(t)$:

$$\begin{aligned} \Delta V_{\rm OUT} &= V_{\rm OUT|\,without\ field} - V_{\rm OUT|\,with\ field} \\ &= \frac{V_B}{C_F} \int \frac{1}{R_0 + \Delta R\,(t)} - \frac{1}{R_0} dt \\ &\cong -\frac{V_B}{R_0^2 C_F} \int \Delta R\,(t)\, dt. \end{aligned} \qquad (3)$$

The equivalent schematic for noise analysis is shown in Fig. 5(b). Since the parasitic capacitance at the inverting node of the op-amp is much smaller than $C_{\rm F}$, reset noise of the integrator is negligible [33]. In addition to the sensor under test $R_{\rm S}$, all other sensors $R_{\rm S1} - R_{\rm S7}$ in the same row contribute to the noise due to the matrix configuration. The noises contributed by $V_{\rm CM}$, $V_{\rm IN}$, and $V_{\rm INB}$ are experimentally verified to be negligible due to their low bandwidth. Hence, the output-referred noise can be derived as follows:

$$\begin{aligned} v_{\rm n,out}^2 &= \left(\frac{1}{2\pi f C_{\rm F}}\right)^2 \left(8 {i_{\rm n,Rs}}^2 + \frac{4kT}{R_{\rm D}}\right) \\ &\quad + \left(\frac{9}{2\pi f R_{\rm S} C_{\rm F}} + 1\right)^2 {v_{\rm n,op}}^2 \end{aligned} \qquad (4)$$

where $i_{\rm n,Rs}$ represents the current noise contributed by each sensor, $v_{\rm n,op}$ represents the voltage noise contributed by the op-amp, k is the Boltzmann constant, T is the temperature, and f is the frequency. Both $i_{\rm n,Rs}$ and $v_{\rm n,op}$ include white and $1/f$ noise.

D. Electromagnet Driver

The finite switching time of the magnetic field results in a deadzone where measurements cannot be taken. To minimize the deadzone time to detect MNPs with fast relaxation times, the switch-off response of magnetic field needs to be as fast as possible. However, this requirement is at odds with typical methods of generating magnetic fields that result in large inductances. Both stripelines [34] and miniaturized coils [35], [36] have been used for achieving a fast switch-off response due to their low inductance. However, stripelines are incapable of generating large magnetic fields (3.2 Oe in [34]) and lose control over the field uniformity, and miniaturized coils require complex micromachining techniques. Helmholtz coils, on the other hand, generate homogeneous in-plane fields, are easy to fabricate, and facilitate proper sensor alignment due to their geometry [37]–[39]. However, the large inductance of a Helmholtz coil limits the bandwidth, making the fast switching difficult.

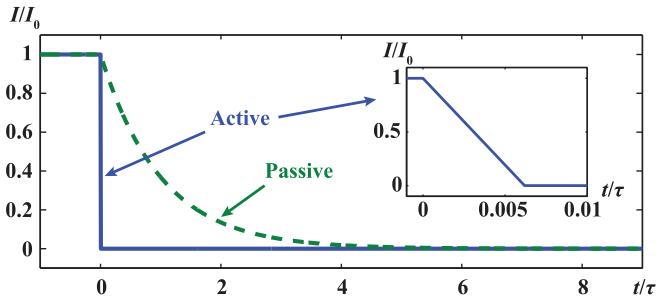

Fig. 6. Comparison of energy dissipation techniques.

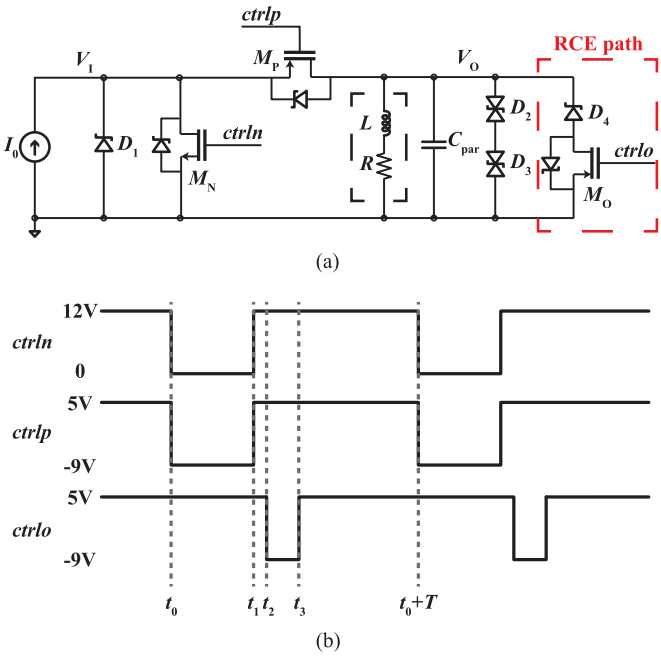

Fig. 7. (a) Schematic of electromagnet driver implementing active discharge. (b) Timing diagram of control signals.

There are two methods to discharge the stored energy in an electromagnet: passively and actively. To passively discharge the electromagnet, both sides of the electromagnet are placed at the same potential and the current in the electromagnet can be written as: $I(t) = I_0 \exp(-t/\tau)$, where I_0 is the initial current, $\tau = L/R$ is the time constant, and t is time. Given that Helmholtz coils usually have large L and small R by design, this results in a large τ and slow decay of the current. Alternatively, the energy can be actively removed by connecting a negative voltage source V, accordingly $I(t) = I_0 - (V/L)t$. With a large enough V, this technique can rapidly remove the energy stored in the electromagnet within 0.006τ, ∼1,000× faster (Fig. 6).

Based on the active discharge technique, a novel electromagnet driver was designed, as shown in Fig. 7(a). To the first order, the electromagnet can be modeled as an inductor in series with a resistor. The driver is operated in two phases and controlled by pulse width modulation (PWM) signals *ctrln* and *ctrlp* through power MOSFET switches $M_{\rm N}$ and $M_{\rm P}$. The reverse current

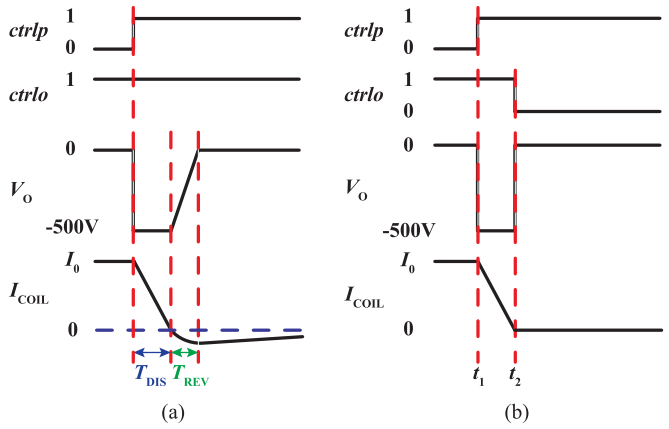

Fig. 8. (a) Reverse current due to parasitic capacitance. (b) RCE path eliminates the reverse current.

elimination (RCE) path, which consists of $M_{\rm O}$, *ctrlo*, and D_4, will be discussed later.

As shown in Fig. 7(b), during the charge phase ($t_0 - t_1$), *ctrln* and *ctrlp* are low, therefore $M_{\rm N}$ is off and $M_{\rm P}$ is on. A DC current I_0 flows into the electromagnet through $M_{\rm P}$. To discharge the electromagnet (at time $t_1 - t_0 + T$), *ctrln* and *ctrlp* are high, therefore $M_{\rm N}$ is on and $M_{\rm P}$ is off. Transient voltage suppression (TVS) diodes D_2 and D_3 clamp $V_{\rm O}$ at a negative voltage of –500 V, which generates a low impedance path to rapidly remove the stored energy. While the negative voltage should be as large as possible to achieve a fast switch-off response, it is limited by both the electromagnet breakdown voltage and the drain-source breakdown voltage of $M_{\rm P}$. Meanwhile, I_0 flows to ground through $M_{\rm N}$, and diode D_1 protects $M_{\rm N}$ and the current source from large transient voltage spikes.

The proposed topology can speed up the switch-off response significantly, but comes with a reverse current, as shown in Fig. 8(a). After the energy stored in the coil has been fully dissipated, $V_{\rm O}$ is expected to rise back to 0 V. However, the parasitic capacitance $C_{\rm par}$ from the electromagnet, TVS diodes, MOSFET $M_{\rm P}$, and PCB prevents $V_{\rm O}$ from instantly returning to 0 V. Since there is no external source to charge $C_{\rm par}$, current is pulled out of the coil during $T_{\rm REV}$. Therefore, after $I_{\rm COIL}$ drops down to 0 A, the negative $V_{\rm O}$ continues "discharging" the electromagnet, resulting in a reverse current whose magnitude keeps increasing until $V_{\rm O}$ reaches 0 V. Making this issue worse, as $|V_{\rm O}|$ decreases from 500 V to 0 V, the low-impedance path generated by D_2 and D_3 is broken. The reverse current must be dissipated as heat by the electromagnet resistance and thus lingers for a comparatively long time. This phenomenon was observed experimentally and was also discussed in [40]. In our application, this reverse current and the associated magnetic field is not acceptable as it magnetizes the MNPs, instead of allowing them to relax to equilibrium.

Our solution is to reduce $T_{\rm REV}$ by forcing $V_{\rm O}$ to 0 V. To facilitate this, an RCE path is added at the output node in parallel with the electromagnet and TVS diodes, as shown in Fig. 7(a). The RCE path operates as follows: as soon as the energy in the electromagnet is fully dissipated, $M_{\rm O}$ is turned on, providing an alternative low-impedance path to charge $C_{\rm par}$. This pulls $V_{\rm O}$ back to 0 V quickly, eliminating the reverse current. D_4 is needed to prevent unwanted current flow during the charge phase. The signal timing is illustrated in Fig. 8(b). It should be noted that the turn-on time (at $t_1 - t_2$) is nearly equal to the coil switch-off time, given that the rise and fall time of these signals are similar as confirmed through simulation and verified experimentally.

The timing of *ctrlo* is critical and requires a sub-microsecond resolution for microsecond field switching times. Early turn-on causes $V_{\rm O}$ to start returning to 0 V too early when the energy stored in the electromagnet has not been fully dissipated. Without a large negative $V_{\rm O}$, the residual current will decay exponentially with time constant of L/R, resulting in a long switch-off time. On the other hand, if *ctrlo* arrives late, the reverse current cannot be fully removed.

While inductor-current zero-crossing detection methods have been demonstrated to achieve high-accuracy timing control [41], [42], they all require additional detection circuits. In our case, the zero-crossing detector is not needed since the correct timing can be derived as follows:

$$t = t_{\rm os} + \frac{I_0 L}{|V_{\rm m}|} \tag{5}$$

where $t_{\rm os}$ is the offset time, which is determined by the circuit delay, I_0 is the current flowing into the electromagnet, L is the electromagnet inductance, and $V_{\rm m}$ is the output voltage during switching-off, which is 500 V in our design.

For a given electromagnet, L and $V_{\rm m}$ are fixed. To use (5) to calculate the turn-on delay t based on a given current I_0, the offset time $t_{\rm os}$, which is highly dependent on the electromagnet parasitic capacitance, must be measured. The measurement procedure is as follows:

1) Choose a current value I_0, turn $M_{\rm O}$ off, and measure how long it takes $I_{\rm COIL}$ to drop to 0 A.
2) With this time as $M_{\rm O}$ turn-on time, verify that the reverse current has been eliminated.
3) Calculate $t_{\rm os}$ using the known parameters.

This calibration procedure only needs to be done once per electromagnet to determine $t_{\rm os}$, after which the timing can be calculated for different current values.

In addition to the electromagnet driver, optimizing the Helmholtz coil is critical to further improve the switch-off speed. The magnetic field generated by a Helmholtz coil and the inductance of the Helmholtz coil can be derived as follows:

$$H = 10^4 (0.8)^{2/3} \frac{\mu_0 n I}{R} \tag{6}$$

$$L = \frac{2R^2 n^2}{9R + 10W} \tag{7}$$

where H is the magnetic field intensity in Oe, L is the inductance, R is the radius of each coil, n is the number of turns, μ_0 is the permeability of free space, and W is the distance between the two coils. By combining (5)–(7), the switch-off time can be derived as follows:

$$t = t_{\rm os} + \frac{2R^3 H n}{10^4 (0.8)^{2/3} \mu_0 V_m \, (9R + 10W)} \tag{8}$$

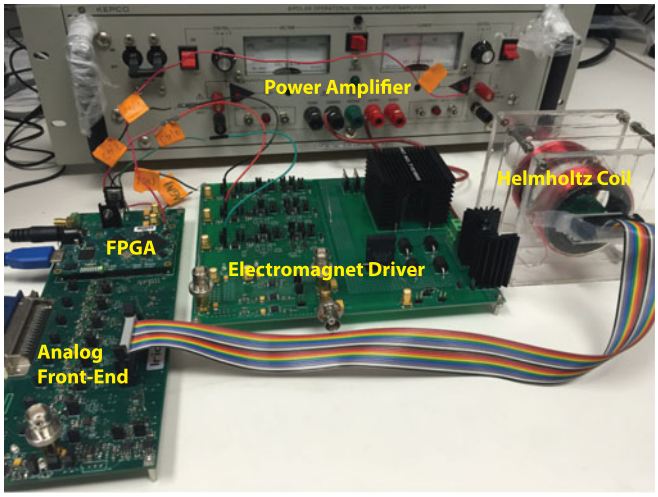

Fig. 9. Photograph of the measurement setup.

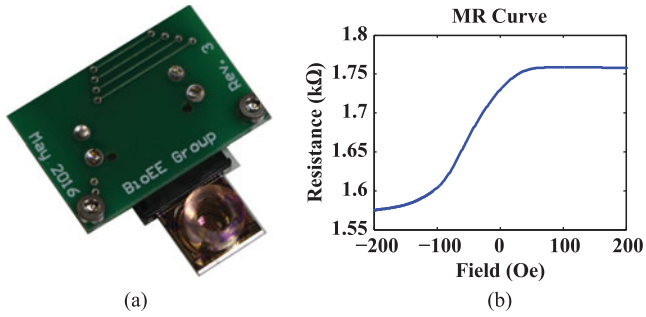

Fig. 10. (a) Photograph of the GMR sensor chip. (b) Measured magnetoresistance curve of the GMR sensor.

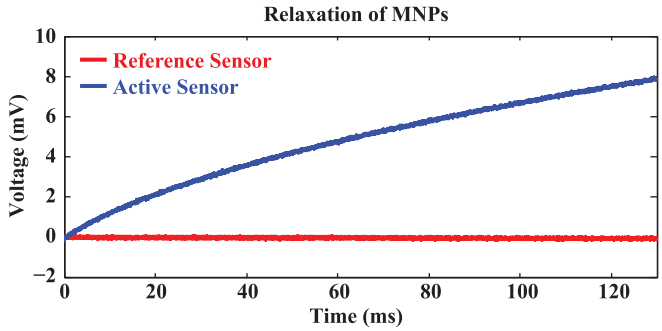

Fig. 11. Relaxation signal of dried MNPs.

Therefore, for a fixed magnetic field, fewer turns, and/or a smaller radius result in faster switching time. However, the minimum radius is dictated by the sensor size. Fewer turns results in lower inductance and larger current with the maximum current usually limited by the heat dissipation.

III. System Implementation

This system was implemented using an FPGA (Opal Kelly XEM6310), a National Instruments Data Acquisition Card (DAQ, NI PCIe-6351), a power amplifier (Kepco BOP 36-12ML), a custom designed Helmholtz coil, and two printed circuit boards (PCBs), as shown in Fig. 9. The DAQ has 8 analog input channels with 16-bit ADCs and 2 analog output channels with 16-bit DACs. The input channels were used to acquire the outputs of the integrators and the output channels were used to generate V_{B} for the integrator bias voltage and V_{CTRL} for the PA control voltage. The PA was set to constant current mode and can provide a DC current of up to 12 A. The FPGA was controlled through USB by MATLAB.

The electromagnet driver and the AFE were implemented on separate PCBs to isolate ground currents. The electromagnet driver has low voltage control circuitry on the left side and high power driving circuitry on the right side, separated by a thick and wide ground layer. The critical P-Channel MOSFET M_{P} on the electromagnet driver is a PolarP Power MOSFET (IXYS IXTK32P60P), which can handle 32 A and has a breakdown voltage of 600 V.

The sensor chip (MagArray, Inc.) has an 8×10 array of GMR sensors, each of which is 125 μm $\times$ 125 μm. It was positioned in the center of the electromagnet and connected to the AFE with a ribbon cable. The op-amps (Analog Devices, Inc. AD8655) for the switched integrators have rail-to-rail input/output. The feedback capacitors C_{F} are 0.68 μF film capacitors, since film capacitors have a lower voltage coefficient than ceramic capacitors. The discharge resistors R_{D} were set to 1.8 kΩ slightly larger than the sensor range.

IV. Experimental Results and Discussion

The system was thoroughly characterized, first by verifying the sensors and measuring the noise, which allows further optimization for maximum SNR. We then characterized the ultrafast switching and RCE technique using two different electromagnets. Moreover, it was verified that the MCDS technique improved the system performance by reducing non-linearity and temperature drift. Lastly, the relaxation signal of commercially available MNPs was measured and an immunoassay was run.

A. GMR Sensor Characterization

The GMR sensors were characterized without MNPs by measuring the magnetoresistance (MR) curve. The external field was swept from -200 Oe to 200 Oe at a rate of 1 Oe/s. The sensor resistance as a function of field is shown in Fig. 10. The nominal resistance in the array ranged from 1.6 kΩ to 1.75 k Ω with an average sensitivity of $\sim 1\,\Omega/\mathrm{Oe}$.

B. Magnetorelaxation Detection of Dried MNPs

To validate the concept, MNPs (Ocean Nano-Technologies SHS-30-01) with a core size of 30 nm were dried on the surface of the sensors. Part of the sensor chip was covered with epoxy to serve as a negative control. Fig. 11 shows two representative sensors, an active sensor with MNPs and a reference sensor without. The active sensor exhibited a relaxation signal with amplitude of $\sim$8 mV, while the reference sensor had no signal.

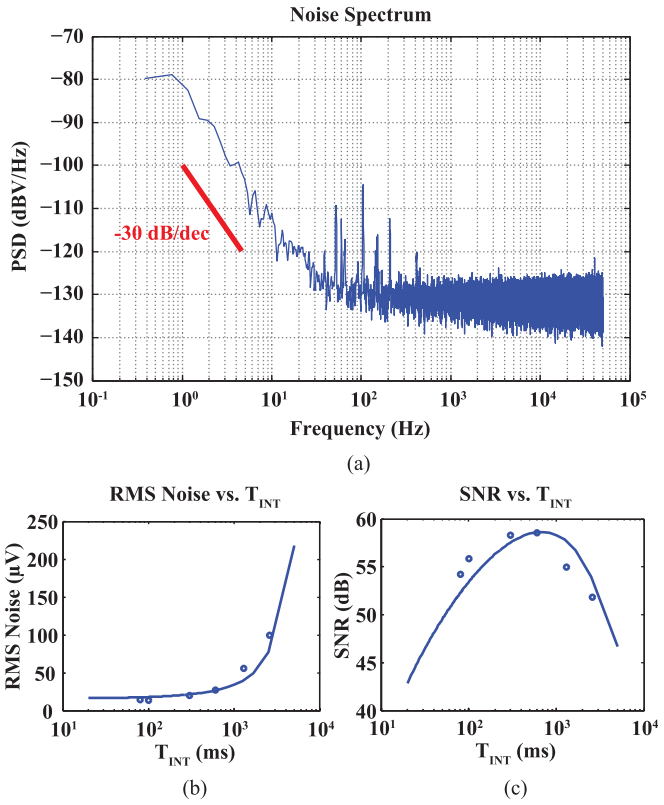

Fig. 12. Noise performance of system showing (a) Noise spectrum for $T_{\rm INT} = 2.6$ s, (b) Simulated and measured RMS noise vs. $T_{\rm INT}$, and (c) Simulated and measured SNR vs. $T_{\rm INT}$.

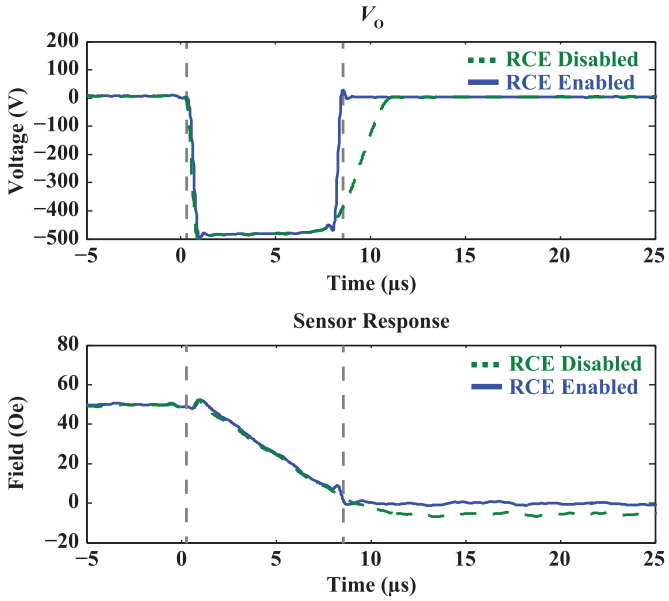

Fig. 13. Measurement results showing the reverse current elimination (RCE) technique.

C. Noise Analysis and Measurement

To optimize the SNR of the system, consider (3) and (4). $R_{\rm D}$ is required to be close to R_0 for current cancellation and therefore cannot be changed. Increasing $C_{\rm F}$ reduces both the signal and noise. Increasing $V_{\rm B}$ improves the SNR, but is limited by the breakdown voltage of the sensor. On the other hand, both $C_{\rm F}$ and $V_{\rm B}$ affect the integration time $T_{\rm INT}$. While increasing $T_{\rm INT}$ increases the signal amplitude because there is more time to integrate the relaxation signal, it also increases the integrated noise by reducing the lower limit of integration $f_{\rm min}$, where $f_{\rm min} = 1/T_{\rm INT}$. Hence, for a given sensor and MNP relaxation time, there exists an optimum $T_{\rm INT}$.

The noise contributed by a sensor and op-amp were measured to be $i_{\rm n,Rs} = 3.2\ {\rm pA}/\sqrt{\rm Hz}$ and $v_{\rm n,op} = 2.7\ {\rm nV}/\sqrt{\rm Hz}$, respectively. Both noise sources have a $1/f$ corner frequency of $\sim$1 kHz. Using (4) with these values, it turns out that $1/f$ noise is dominant below 10 kHz. Through subtracting integration curves in adjacent cycles, the noise in the integration phase can be extracted. To observe low frequency band, $T_{\rm INT}$ was extended to 2.6 s by decreasing $V_{\rm B}$. In Fig. 12(a), although the high frequency band was limited by the ADC quantization noise, the low frequency band has a slope of -30 dB/dec, which matches with the theoretical analysis.

Due to the limitation on $C_{\rm F}$, the relaxation signal under large $T_{\rm INT}$ but the same $V_{\rm B}$ cannot be measured. To analyze SNR for different $T_{\rm INT}$ to find the optimum, simulated relaxation signals were calculated based on (1). Since parameters C and $t_{\rm C}$ are unknown in (1), the simulated signal was first fitted to the measured signal for $T_{\rm INT} = 100$ ms to extract the parameters. Then, the signal was estimated for different $T_{\rm INT}$ up to 5 s.

Since multiple cycles were used for signal averaging and $T_{\rm INT}$ would affect the number of cycles to average, a fixed measurement time of 60 s was applied for noise and SNR tests. It should be noted that MCDS requires two measurement cycles (one with field and one without field) to extract one processed cycle, and there is a gap of 0.6 s between integration curves in adjacent measurement cycles. Therefore, the sampled data in adjacent processed cycles were separated by the time of $2T_{\rm CYC} = 2 \times (T_{\rm INT} + 0.6)$ s. This time was long enough to ignore the correlation of $1/f$ noise, therefore both white noise and 1/*f* noise could be reduced through signal averaging. The simulated (lines) and measured (dots) noise and SNR vs. $T_{\rm INT}$ are shown in Fig. 12(b) and (c), respectively. The optimum $T_{\rm INT}$ was found to be 600 ms. Since the data with MCDS enabled is uncorrelated, signal averaging can be used to reduce the noise variance.

D. Electromagnet Driver Switch-off Response

The performance of the electromagnet driver switch-off response was measured using both a GMR sensor and an oscilloscope (Tektronics TDS2014C). By biasing the sensor with a DC current, the transient response of sensor was captured to monitor the magnetic field. The bandwidth of the GMR sensor, bias circuit, and oscilloscope was measured to be much higher than the switch-off response of the magnetic field.

To illustrate the performance improvement of the RCE technique, measurements with the RCE enabled and disabled are presented in Fig. 13. It can be observed that the RCE forced $V_{\rm O}$ back to 0 V rapidly when enabled. Thus, the reverse current,

TABLE I
COMPARISON OF DIFFERENT ELECTROMAGNETS

Parameter	Coil 1	Coil 2
Inductance L	1.5 mH	80 μH
Current I_0	2 A	8 A
Physical Size (W × L × H)	10 × 8 × 10 cm^3	15 × 59 × 23 cm^3
Time Constant τ	600 μs	1,600 μs
Switch-off Time	8.5 μs	1.4 μs
Switch-off Speed	5.9 Oe/μs	35.7 Oe/μs
Improvement	71×	1,142×

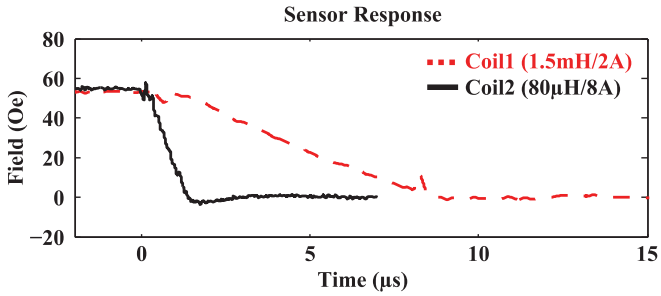

Fig. 14. Measurement results for comparison between two coils.

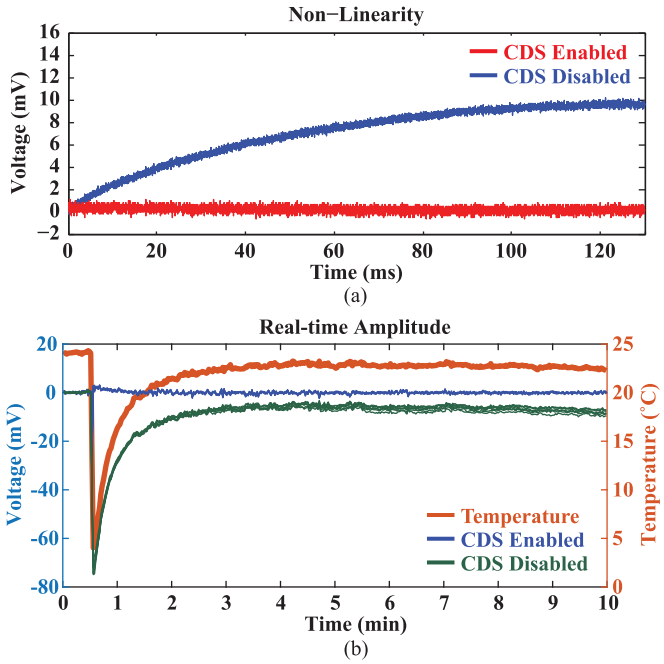

Fig. 15. (a) Non-linearity and (b) temperature sensitivity improvement from MCDS technique.

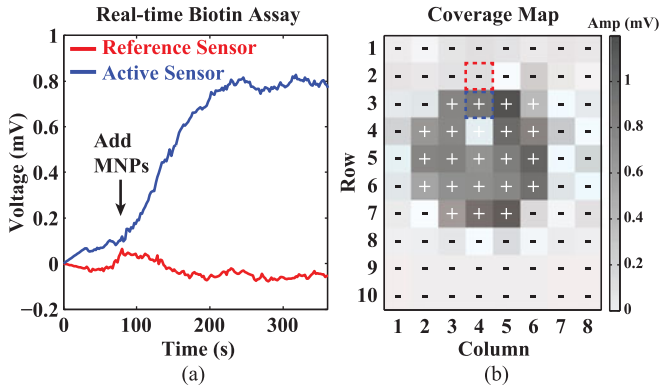

Fig. 16. (a) Real-time biotin assay experiment. (b) Post-assay full chip scan and signal amplitudes.

which caused a reverse magnetic field of up to −10 Oe and took 500 μs to dissipate, was fully removed. To verify the electromagnet optimization, two Helmholtz coils were custom designed, as summarized in Table I. The currents in both were set to achieve a magnetic field of 50 Oe. Fig. 14 shows the measurement results obtained from each of the electromagnets. The switch-off speed of Coil 2 (35.7 Oe/μs), which had lower inductance and higher current, was faster than Coil 1 (5.9 Oe/μs), supporting the electromagnet design principle stated earlier. However, Coil 2 requires 4× higher current and a cooling fan for proper heat dissipation resulting in a larger physical size. Compared with the natural exponential decay time constant τ, the switch-off speeds for both coils were improved significantly enabling MNPs with relaxation times of only a few microseconds to be detected.

E. Magnetic Correlated Double Sampling Validation

The large voltage swing at V_{OUT} from V_{CM} to 0 V during the integration phase causes non-linearity from both the op-amp and the feedback capacitor. To illustrate this, a measurement was taken using a GMR sensor with no MNPs, as shown in Fig. 15(a). The non-linearity was extracted by subtracting the measured data from a linear fit of the curve. Without MCDS, the non-linearity is ∼10 mV, which is comparable to the relaxation signal amplitude and similar in shape. After applying MCDS, the non-linearity is eliminated below the noise level. Similarly, the standard deviation of the sensor resistance on the same chip was measured to be 5.9 Ω and reduced to 0.86 mΩ (99.98%) with MCDS.

While the non-linearity is constant over time, environmental variation such as temperature drift is not. This is illustrated in Fig. 15(b) where the temperature and amplitude of 7 sensors are plotted over time. 20 μL deionized (DI) water stored in the refrigerator (4 °C) was added at $t = 40$ s, and the temperature was indirectly calculated from R_0. The signals without MCDS show a strong correlation with the temperature whereas MCDS significantly reduces the temperature dependence. It should be noted that there is a single-point spike when the water was added since it occurred in the middle of an MCDS cycle.

F. Magnetic Immunoassay

Lastly, the experiment was extended from dried MNPs to an immunoassay. The sensor chip was partially functionalized with biotin and subsequently blocked with bovine serum albumin (BSA). The biotin on the active sensors binds with the streptavidin conjugated MNPs whereas the reference sensors were used to monitor non-specific binding. This experiment was performed with real-time measurement to observe the binding kinetics, as shown in Fig. 16(a). The MNPs were added at $t = 80$ s and

the experiment lasted until the binding plateaued. The sensors were then washed with phosphate-buffered saline (PBS) three times to remove unbound MNPs. The reference sensors and the washing step showed no change in signal amplitude indicating minimal non-specific binding. The full chip results are shown in Fig. 16(b) with the active sensors denoted by a $+$ and the reference sensors by a $-$. The red and blue dotted squares indicate the reference sensor and the active sensor in the real-time measurement, respectively. The variation in amplitude for the active sensors was the result of the MNP surface coverage, which could be improved using individual spot functionalization versus the blanket functionalization procedure used here.

V. Conclusion

In this paper, a MRX biosensor system was demonstrated to detect the relaxation of 30 nm MNPs. A switched integrator was designed to integrate the relaxation signal with time, relaxing the bandwidth requirement of the ADC. An ultrafast electromagnet driver that actively dissipates the stored energy in the Helmholtz coil was designed to reduce the deadzone time. A magnetic correlated double sampling technique effectively eliminates the sensor-to-sensor variation, temperature drift, circuit offset and non-linearity. Measurement results for the electromagnet driver with a custom designed electromagnet show a fast switch-off response of >5 Oe/μs. The experimental results of dried MNPs show that the relaxation of particles can be successfully detected and the biotin-BSA immunoassay demonstrates it is also possible to monitor the binding kinetics in real-time. This work lays the foundation for a fast and sensitive biosensing for point-of-care diagnostics platform.

References

[1] A. C. Fernandes, C. M. Duarte, F. A. Cardoso, R. Bexiga, S. Cardoso, and P. P. Freitas, "Lab-on-chip cytometry based on magnetoresistive sensors for bacteria detection in milk," *Sensors*, vol. 14, no. 8, pp. 15496–15524, Aug. 2014.

[2] A. Chicharo, F. Cardoso, S. Cardoso, and P. P. Freitas, "Dynamical detection of magnetic nanoparticles in paper microfluidics with spin valve sensors for point-of-care applications," *IEEE Trans. Magn.*, vol. 50, no. 11, Nov. 2014, Art. no. 5102204.

[3] N. Sun, T. J. Yoon, H. Lee, W. Andress, R. Weissleder, and D. Ham, "Palm NMR and 1-chip NMR," *IEEE J. Solid-State Circuits*, vol. 46, no. 1, pp. 342–352, Jan. 2011.

[4] H. Shao *et al.*, "Magnetic nanoparticles and microNMR for diagnostic applications," *Theranostics*, vol. 2, no. 1, pp. 55–65, Jan. 2012.

[5] D. Issadore, C. Min, M. Liong, J. Chung, R. Weissleder, and H. Lee, "Miniature magnetic resonance system for point-of-care diagnostics," *Lab. Chip*, vol. 11, no. 13, pp. 2282–2287, Jul. 2011.

[6] M. Piedade *et al.*, "A new hand-held microsystem architecture for biological analysis," *IEEE Trans. Circuits Syst., Reg. Papers*, vol. 53, no. 11, pp. 2384–2395, Nov. 2006.

[7] R. L. Edelstein *et al.*, "The BARC biosensor applied to the detection of biological warfare agents," *Biosens. Bioelectron.*, vol. 14, no. 10/11, pp. 805–813, Jan. 2000.

[8] R. S. Gaster, D. A. Hall, and S. X. Wang, "nanoLAB: An ultraportable, handheld diagnostic laboratory for global health," *Lab. Chip*, vol. 11, no. 5, pp. 950–956, Mar. 2011.

[9] O. Florescu, M. Mattmann, and B. Boser, "Fully integrated detection of single magnetic beads in complementary metal-oxide-semiconductor," *J. Appl. Phys.*, vol. 103, no. 4, Feb. 2008, Art. no. 46101.

[10] H. Wang, Y. Chen, A. Hassibi, A. Scherer, and A. Hajimiri, "A frequency-shift CMOS magnetic biosensor array with single-bead sensitivity and no external magnet," in *Proc. 2009 IEEE Int. Solid-State Circuits Conf. Dig. Tech. Papers*, 2009, pp. 438–439, 439a.

[11] W. Wang, Y. Wang, L. Tu, Y. Feng, T. Klein, and J.-P. Wang, "Magnetoresistive performance and comparison of supermagnetic nanoparticles on giant magnetoresistive sensor-based detection system," *Sci. Rep.*, vol. 4, Jul. 2014, Art. no. 5716.

[12] H. J. Chung, C. M. Castro, H. Im, H. Lee, and R. Weissleder, "A magneto-DNA nanoparticle system for rapid detection and phenotyping of bacteria," *Nature Nanotechnol.*, vol. 8, no. 5, pp. 369–375, May 2013.

[13] H. J. Hathaway *et al.*, "Detection of breast cancer cells using targeted magnetic nanoparticles and ultra-sensitive magnetic field sensors," *Breast Cancer Res.*, vol. 13, 2011, Art. no. R108.

[14] R. S. Gaster *et al.*, "Matrix-insensitive protein assays push the limits of biosensors in medicine," *Nature Med.*, vol. 15, no. 11, pp. 1327–1332, Nov. 2009.

[15] V. C. Martins *et al.*, "Femtomolar limit of detection with a magnetoresistive biochip," *Biosens. Bioelectron.*, vol. 24, no. 8, pp. 2690–2695, Apr. 2009.

[16] D. L. Graham, H. Ferreira, J. Bernardo, P. P. Freitas, and J. M. S. Cabral, "Single magnetic microsphere placement and detection on-chip using current line designs with integrated spin valve sensors: Biotechnological applications," *J. Appl. Phys.*, vol. 91, no. 10, pp. 7786–7788, May 2002.

[17] C. R. Tamanaha, S. P. Mulvaney, J. C. Rife, and L. J. Whitman, "Magnetic labeling, detection, and system integration," *Biosens. Bioelectron.*, vol. 24, no. 1, pp. 1–13, Sep. 2008.

[18] L. Li, K. Y. Mak, C. W. Leung, S. M. Ng, Z. Q. Lei, and P. W. T. Pong, "Detection of 10-nm superparamagnetic iron oxide nanoparticles using exchange-biased GMR sensors in wheatstone bridge," *IEEE Trans. Magn.*, vol. 49, no. 7, pp. 4056–4059, Jul. 2013.

[19] J. Xu *et al.*, "Detection of the concentration of MnFe2O4 magnetic microparticles using giant magnetoresistance sensors," *IEEE Trans. Magn.*, vol. 52, no. 4, Apr. 2016, Art. no. 5200204.

[20] D. A. Hall *et al.*, "GMR biosensor arrays: A system perspective," *Biosens. Bioelectron.*, vol. 25, no. 9, pp. 2051–2057, May 2010.

[21] D. A. Hall, R. S. Gaster, K. A. A. Makinwa, S. X. Wang, and B. Murmann, "A 256 pixel magnetoresistive biosensor microarray in 0.18 um CMOS," *IEEE J. Solid-State Circuits*, vol. 48, no. 5, pp. 1290–1301, May 2013.

[22] W. F. Brown, "Thermal fluctuations of a single-domain particle," *Phys. Rev.*, vol. 130, no. 5, pp. 1677–1686, Jun. 1963.

[23] F. Ludwig, E. Heim, and M. Schilling, "Magnetorelaxometry of magnetic nanoparticles—A new method for the quantitative and specific analysis of biomolecules," in *Proc. 4th IEEE Conf. Nanotechnol.*, 2004, pp. 245–248.

[24] L. Néel, "Théorie du traînage magnétique des substances massives dans le domaine de Rayleigh," *J. Phys. Radium*, vol. 11, no. 2, pp. 49–61, 1950.

[25] R. W. Chantrell, S. R. Hoon, and B. K. Tanner, "Time-dependent magnetization in fine-particle ferromagnetic systems," *J. Magn. Magn. Mater.*, vol. 38, no. 2, pp. 133–141, Sep. 1983.

[26] A. P. Astalan, F. Ahrentorp, C. Johansson, K. Larsson, and A. Krozer, "Biomolecular reactions studied using changes in Brownian rotation dynamics of magnetic particles," *Biosens. Bioelectron.*, vol. 19, no. 8, pp. 945–951, Mar. 2004.

[27] P. P. Liu *et al.*, "Magnetic relaxation detector for microbead labels," *IEEE J. Solid-State Circuits*, vol. 47, no. 4, pp. 1056–1064, Apr. 2012.

[28] S. Gambini *et al.*, "A CMOS 10kpixel baseline-free magnetic bead detector with column-parallel readout for miniturized immunoassays," in *Proc. IEEE Int. Solid-State Circuits Conf. Dig. Tech. Paper*, Feb. 2012, pp. 126–128.

[29] N. L. Adolphi *et al.*, "Characterization of magnetite nanoparticles for SQUID-relaxometry and magnetic needle biopsy," *J. Magn. Magn. Mater.*, vol. 321, no. 10, pp. 1459–1464, May 2009.

[30] H. C. Bryant *et al.*, "Magnetic properties of nanoparticles useful for SQUID relaxometry in biomedical applications," *J. Magn. Magn. Mater.*, vol. 323, no. 6, pp. 767–774, Mar. 2011.

[31] E. Romanus *et al.*, "Magnetic nanoparticle relaxation measurement as a novel tool for in vivo diagnostics," *J. Magn. Magn. Mater.*, vol. 252, pp. 387–389, Nov. 2002.

[32] D. A. Hall, R. S. Gaster, S. J. Osterfeld, B. Murmann, and S. X. Wang, "GMR biosensor arrays: Correction techniques for reproducibility and enhanced sensitivity," *Biosens. Bioelectron.*, vol. 25, no. 9, pp. 2177–2181, May 2010.

[33] B. Bechen, A. Kemna, M. Gnade, T. v. d. Boom, and B. Hosticka, "Noise considerations of integrators for current readout circuits," *Adv. Radio Sci.*, vol. 3, pp. 331–336, May 2005.

[34] T. Korn, F. Müller, D. Grundler, and C. Schüller, "Characterization of permalloy films on high-bandwidth striplines," *J. Magn. Magn. Mater.*, vol. 272–276, suppl., pp. E1341–E1342, May 2004.

[35] Ł. Pawliszak, M. Tekielak, and M. Zgirski, "Miniature coils for producing pulsed inplane magnetic fields for nanospintronics," *Rev. Sci. Instrum.*, vol. 86, no. 3, Mar. 2015, Art. no. 34711.
[36] K. Mackay, M. Bonfim, D. Givord, and A. Fontaine, "50 T pulsed magnetic fields in microcoils," *J. Appl. Phys.*, vol. 87, no. 4, pp. 1996–2002, Feb. 2000.
[37] S. S. Jian Wang, "An improved Helmholtz coil and analysis of its magnetic field homogeneity," *Rev. Sci. Instrum.*, vol. 73, no. 5, pp. 2175–2179, 2002.
[38] I. Sasada and Y. Nakashima, "Planar coil system consisting of three coil pairs for producing a uniform magnetic field," *J. Appl. Phys.*, vol. 99, no. 8, Apr. 2006, Art. no. 08D904.
[39] M. S. Crosser, S. Scott, A. Clark, and P. M. Wilt, "On the magnetic field near the center of Helmholtz coils," *Rev. Sci. Instrum.*, vol. 81, no. 8, Aug. 2010, Art. no. 84701.
[40] E. Mori, "Ultra fast and high efficiency inductive coil driver," U.S. Patent US6670796 B2, Dec. 30, 2003.
[41] G. Villar and E. Alarcon, "Inductor-current zero-crossing detection mixed-signal CMOS circuit for a DCM-operated 3-level switching power converter," in *Proc. IEEE Int. Symp. Circuits Syst.*, 2008, pp. 2606–2609.
[42] V. Michal, "Inductor current zero-crossing detector and CCM/DCM boundary detector for integrated high-current switched-mode DC-DC converters," *IEEE Trans. Power Electron.*, vol. 29, no. 10, pp. 5384–5391, Oct. 2014.

Xiahan Zhou received the B.S. degree in microelectronics technology from the University of Electronic Science and Technology of China, Chengdu, China, in 2012, and the M.S. degree (with honors) in electrical engineering from the University of Southern California, Los Angeles, CA, USA, in 2014. He is currently working toward the Ph.D. degree in electrical and computer engineering at the University of California, San Diego, CA, USA.

His research interests include analog and mixed-signal circuits and systems for medical devices, biosensors, and biomedical applications.

Chih-Cheng Huang received the B.S. degree in materials science and engineering from National Taiwan University, Taipei, Taiwan, in 2010, and the M.S. degree in nanoengineering from National Tsing Hua University, Hsinchu, Taiwan, in 2012. He is currently working toward the Ph.D. degree in materials science at the University of California, San Diego, CA, USA.

His research interests include magnetoresistive materials, biosensors, and proteomics.

Drew A. Hall (S'07–M'12) received the B.S. degree in computer engineering with honors from the University of Nevada, Las Vegas, NV, USA, in 2005, and the M.S. and Ph.D. degrees in electrical engineering from Stanford University, Stanford, CA, USA, in 2008 and 2012, respectively.

From 2011 to 2013, he was a Research Scientist in the Integrated Biosensors Laboratory at Intel Corporation. Since 2013, he has been with the Department of Electrical and Computer Engineering, University of California at San Diego, as an Assistant Professor. His research interests include bioelectronics, biosensors, analog circuit design, medical electronics, and sensor interfaces.

Dr. Hall received the First Place in the Inaugural International IEEE Change the World Competition and First Place in the BME-IDEA invention competition, both in 2009. He received the Analog Devices Outstanding Designer Award in 2011, an Undergraduate Teaching Award in 2014, the Hellman Fellowship Award in 2014, and an NSF CAREER Award in 2015. He is also a Tau Beta Pi Fellow.